

Accepted Article

This article has been accepted for publication and undergone full peer review but has not been through the copyediting, typesetting, pagination and proofreading process, which may lead to differences between this version and the [Version of Record](#). Please cite this article as [doi: 10.1111/JACE.18071](https://doi.org/10.1111/JACE.18071)

This article is protected by copyright. All rights reserved

## **Models for the behavior of boron carbide in extreme dynamic environments**

K. T. Ramesh

Department of Mechanical Engineering & Hopkins Extreme Materials Institute,  
Johns Hopkins University & Corresponding author

Lori Graham-Brady

Department of Civil and Systems Engineering & Hopkins Extreme Materials  
Institute, Johns Hopkins University

William A. Goddard

Materials and Process Simulation Center, California Institute of Technology

Ryan C. Hurley

Department of Mechanical Engineering & Hopkins Extreme Materials Institute,  
Johns Hopkins University

Mark Robbins

Department of Physics and Astronomy, Johns Hopkins University

Andrew L. Tonge

U.S. Army Combat Capabilities Development Command, Army Research Lab-  
oratory

Amartya Bhattacharjee

Department of Civil and Systems Engineering, Johns Hopkins University

Joel T. Clemmer

Sandia National Laboratory

Qinglei Zeng

Hopkins Extreme Materials Institute, Johns Hopkins University

Weixin Li

Hopkins Extreme Materials Institute, Johns Hopkins University

Yidi Shen

Department of Chemical and Materials Engineering, University of Nevada, Reno  
Qi An

Department of Chemical and Materials Engineering, University of Nevada, Reno  
Nilanjan Mitra

Department of Mechanical Engineering & Hopkins Extreme Materials Institute,  
Johns Hopkins University

### **Abstract**

We describe models for the behavior of hot-pressed boron carbide that is subjected to extreme dynamic environments such as ballistic impact. We first identify the deformation and failure mechanisms that are observed in boron carbide under such conditions, and then review physics-based models for each of these mechanisms and the integration of these models into a single physics-based continuum model for the material. Atomistic modeling relates the composition and stoichiometry to the amorphization threshold, while mesoscale

modeling relates the processing-induced defect distribution to the fracture threshold. The models demonstrate that the relative importance of amorphization and fracture are strongly dependent on the geometry and impact conditions, with the volume fraction of amorphized material being unlikely to be significant until very high velocities ( $\sim 3km/s$ ) are reached for geometries such as ball impact on plates. These connections to the physics thus provide guidelines for the design of improved boron carbide materials for impact applications.

## 1 Introduction and Background

An excellent recent review of the mechanical behavior of boron carbide and the recent literature can be found in the work of Awasthi and Subhash [1]. Our focus is on constitutive models for boron carbide subjected to extreme dynamic loading, with a view towards guiding materials design for these extreme environments. Constitutive models for ceramics under dynamic loading are typically of two types: first, phenomenological models that attempt to fit the measured mechanical behavior, and second, physics-based models that incorporate fracture mechanics. Phenomenological models have the advantage of being computationally efficient and fast-running, while physics-based models have the advantage of being extendable to a wider variety of stress states and strain rates. Excellent examples of phenomenological models in this domain include the works of Johnson, Holmquist, and colleagues [2, 3, 4, 5, 6], as well as models developed broadly for geological and quasibrittle materials such as the Kayenta model [7]. Improved phenomenological models have been recently developed for ceramics under ultrahigh pressures [8, 9]. Examples of physics-based models that address the fracture mechanism include the works of Nemat-Nasser and colleagues [10, 11, 12], Huang and Subhash [13], and Paliwal and Ramesh [14]. We will identify specific models for boron carbide in the literature in subsequent sections.

When a ceramic target is subjected to impact loading, a significant amount of kinetic energy is deposited into a small volume of the target, resulting in the generation of a high energy density in the target material. The high energy density is typically associated with an intense transient stress state and results in the activation of multiple mechanisms within the material. Each of these mechanisms has an associated length scale and timescale, and which mechanism is activated and to what degree depends on the stress state, the available time and the stress or deformation history. Physics-based models for the behavior of the ceramic under such intense loading states should incorporate the physics of these multiple mechanisms in order to provide reasonable predictions under extreme loading conditions

within a specific application. This approach then connects the chemistry and microstructure of the material with the mechanisms and the constitutive model, making possible the design of the material for a specific impact application.

In this work we bring together models that capture specific mechanisms that are known to be activated within boron carbide subjected to extreme dynamic environments. These mechanisms each occur at specific length and timescales and models for each mechanism are described in brief. We then discuss the integration of these mechanism-based models into an integrative model that can be exercised at the continuum scale. Our focus is on providing an overview of the models developed for each scale and showing how they come together into an integrated continuum model, rather than on developing a new model. The intention is to provide the reader with a review of the existing literature but in a form that allows for the greatest utility of the models already developed or under development.

## 2 Identification of key mechanisms

For the purposes of this manuscript, we will consider the impact of a spherical projectile into a plate of boron carbide as the canonical problem of interest. We identify impact velocities of up to two kilometers per second as being the relevant velocities, and assume that the initial temperature of the ceramic is room temperature. Simulations using phenomenological models suggest that these impacts generate pressures in the range of  $0 - 35 \text{ GPa}$ , strain rates of  $10^{-2} - 10^6 \text{ s}^{-1}$ , and shear stresses up to  $10 \text{ GPa}$ , with all of these conditions developed over time frames on the order of microseconds. We refer to this collection of variables and their ranges as a “canonical model,” and use the canonical model to guide the development of our constitutive modeling effort (i.e., the mechanisms of interest to us as the ones observed under these conditions).

A combination of in situ and post impact measurements have identified several key mechanisms that are activated within boron carbide under these conditions. These include amorphization at high pressures [15], massive fracture [16] and fragmentation [17], and granular flow [16]. The effects of temperature on the amorphization mechanism have also been considered using MD simulations, [18] and [19]. Once granular flow begins, we also observe dilation in the ceramic, and this results in the development of porosity. Subsequent loading by compression waves then result in the crushing of the porosity, and so pore compaction must also be incorporated as a potential mechanism.

We now discuss specific models for each of these mechanisms before presenting the integration of these mechanisms into an integrated constitutive

model that can be used at the continuum scale for such impact simulations. We begin with the smallest-scale mechanism, that of amorphization.

## 3 Models for the key mechanisms in boron carbide

### 3.1 Amorphization in Boron Carbide

In order to explain the amorphization of boron carbide ( $B_4C$ ) under stress conditions, many theoretical studies focused on the atomic structural failure that leads to the amorphous shear bands. For instance, Density Functional Theory (DFT) simulations on the deformation of  $B_4C$  under hydrostatic and uniaxial loading suggested that the structure failure arises from the reaction of bent 3-atom chains with nearby icosahedra, leading to the deconstruction of icosahedra and formation of amorphous shear bands found in nanoindentation experiments, thus suggesting that the  $B_4C$  failure initiates from the disassembly of the icosahedra during shear deformation [20, 21, 22, 23]. Continuum models for this mechanism have also been developed. We describe each of these types of models below.

#### 3.1.1 Atomistic model for amorphization

To investigate atomistic mechanisms of amorphization in  $B_4C$ , we applied DFT to investigate the shear deformation of  $(B_{11}C_p)(CBC)$  under ideal shear conditions. It should be noted that DFT shows that the most stable  $B_4C$  single crystal has the form  $(B_{11}C_p)(CBC)$ . We used this to examine the response of  $B_4C$  to shear along 11 plausible slip systems and found that  $(01\bar{1}\bar{1})/[\bar{1}101]$  leads to the lowest critical shear stress among all slip systems. The atomistic failure process along this slip system, shown in Fig. 1, consists of two key steps: (1) at 0.245 shear strain, the B-C bonds between neighboring icosahedra break, resulting in formation of a lone pair on the carbene-like carbon; (2) at 0.348 strain, the C-B-C chain is bent significantly that the positive Lewis acidic B atom in the CBC chain can form a Lewis acid-Lewis base bond to this negative carbene, leading to the disintegration of the icosahedron[24].

Even though quantum mechanics (QM) simulations provide an understanding of the underlying physical phenomena associated with amorphization in the crystal, it should be noted that such QM calculations (<200 atoms) have a spatial scale of 2-3nm, too small to describe the amorphous shear bands (which are observed experimentally to be several nm thick and separated by >20nm). Capturing this behavior requires >200,000 atoms, too big for QM. Therefore, to determine the relationship of amorphous shear bands with brittle failure, we used the ReaxFF reactive force field

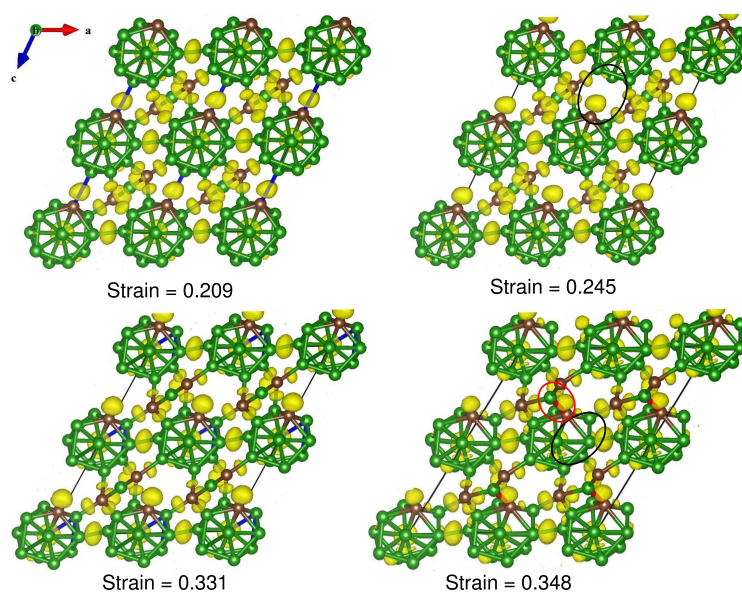


Figure 1: (a) The structures of  $B_4C$  at various strains from DFT calculations, showing the Isosurface of the electron localization functional (ELF). At 0.245 strain, the B-C bond connecting two icosahedra breaks, leading to formation of a negative carbene. At 0.348 strain, this negative carbene reacts with the positive Lewis acidic B atom in the middle of C-B-C chain that has bent way over toward the Carbene C due to the large shear. The green and brown balls represent the boron and carbon atoms, respectively. This figure is from ref.[24].

Accepted Article

in reactive molecular dynamics (RMD) simulations as a function of  $B_4C$  shear deformations for a large  $\sim 200,000$  atom  $B_4C$  crystal that is  $\sim 25$  nm along the x and y directions. This allows sufficient room for forming the 2-3 nm shear bands[25]. We deformed  $B_4C$  along two slip systems:

- $(0001)/[10\bar{1}0]$  which we find favors deformation twinning and
- $(01\bar{1}\bar{1})/[\bar{1}101]$  which we find favors amorphous band formation.

Along the  $(0001)/[10\bar{1}0]$  slip system, we observed first the twinning formation, followed later by amorphous band formation, cavitation, and crack opening, as shown in Fig. 2. We analyzed the RMD trajectory to discover that the origin of the 2-3nm amorphous bands is that they have a 5-10% higher density compared to the crystalline region. This higher density results in tension (negative pressure) that leads to cavitation and crack formation. The density of amorphous region is higher because of more localized bonding character compared to the delocalized bonding within the icosahedron in the crystalline phase. This amorphous band formation was also observed in slip system  $(01\bar{1}\bar{1})/[\bar{1}101]$  where the density of the amorphous band also increases by  $\sim 5\%$ . We caution here that experimental methods have not yet been able to follow the crack initiation in sufficient detail so as to validate the results and interpretations from the theory. Indeed our MD simulations were performed at a high strain rate (over  $10^8 s^{-1}$ ) that could exaggerate the effects, accelerating the transition from twins to cavitation to crack formation. Future experimental and theoretical efforts in this area remain important to follow the initiation and evolution of amorphous bands in boron carbide, particularly at lower strain rates.

In addition, some studies have suggested that temperature increase during shock loading plays an important role in the amorphization of boron carbide [18, 19]. Awasthi and Subhash [18] applied ReaxFF MD simulations to explore the compression process of boron carbide under high-pressure regime of 40-70 GPa, predicting the thermodynamic variables during the amorphization process. Their results indicated that boron carbide will partially or complete melt under such high pressure and cannot recrystallize after cooling. They also predicted the Hugoniot relationship from ReaxFF MD simulations [19], which agreed well with experimental measurements.

Typically in a polycrystal, we encounter multiple grains oriented in various ways with the associated grain boundaries. Grain boundaries (GBs) in  $B_4C$  have been characterized using TEM[26, 27]. To predict the effect of GBs on amorphous band formation, we employed ReaxFF RMD simulations to investigate the deformation mechanisms of nanocrystalline boron carbide (n- $B_4C$ ) with grain sizes ranging from 5 to 15 nm[28]. The finite shear deformations were performed on three polycrystalline models of n- $B_4C$  with average grain sizes of 5nm, 10nm, and 15nm, respectively. The

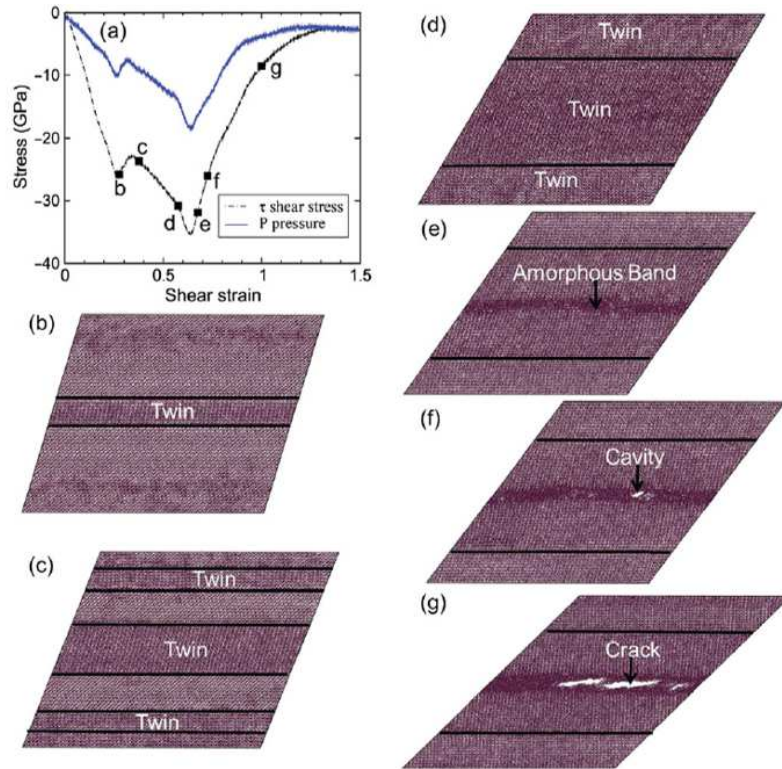


Figure 2: Shear-stress-shear-strain relationship of  $B_4C$  [of form  $(B_{11}C_p)(CBC)$ ] from ReaxFF reactive Molecular Dynamics (RMD) on a single crystal with dimensions of  $\sim 25\text{nm}$  (200,000 atoms) (a) shear along  $(0001)/[10\bar{1}0]$ ; (b)-(g) snapshots during shearing: (b) Twin formation. (c) Twin growth and new twin formation. (d) The growth of the two twins to the whole cell. (e) formation of the 2-3nm Amorphous shear band within the twinned region. (f) Cavitation within the amorphous band. (g) Full crack formation. This figure is from ref.[25].

stress-strain relationships, displayed in Fig. 3(a and b), show that the ideal strength of n-B<sub>4</sub>C decreases as grain size decreases, a reverse Hall-Petch relationship in n-B<sub>4</sub>C. The GB1 model with the smallest grain size (5 nm) has a relatively large plastic deformation (0.25 - 0.5 shear strain) before failure, showing that it is more ductile than the 10nm and 15nm GB models. Our analyses of the deformation mechanism shows that the plastic deformation in n-B<sub>4</sub>C models is dominated by intergranular fracture resulting from GB sliding, as shown in Fig. 6(c, d, and e). In the GB1 model, a larger plastic deformation region arises from a larger fraction of fractured icosahedra along the GBs, leading to high-energy GBs. This deformation mechanism (GB sliding) in n-B<sub>4</sub>C is confirmed by TEM observations[28]. Our simulation results indicate that high-energy GBs in B<sub>4</sub>C help promote GB sliding and plastic deformation, leading to enhanced fracture toughness. Overall the simulations show that smaller grain size substantially increases ductility with only a small decrease in strength.

With the intent of mitigating the adverse effects of amorphization in B<sub>4</sub>C subjected to shear loading, we used QM to examine substitutions of these CBC chains with two atom chains such as Si-Si[29], PP[30], OO[31] (note, it has been demonstrated before that the fundamental cause of B<sub>4</sub>C brittle fracture is the reaction of the middle B in the CBC chains). Indeed the QM shows that (B<sub>11</sub>C)(SiSi) and (B<sub>11</sub>C)(PP) leads to very ductile materials, with the single crystal staying stable as the shear is continued to large strains [29, 30, 31]. Unfortunately the standard techniques for fabricating B<sub>4</sub>C do not lead to incorporating Si-Si chains. However we find that boron rich boron Carbide, B<sub>13</sub>C<sub>2</sub>, [(B<sub>11</sub>C)(BBC)] leads to bent BBC chains[32]. Thus it is possible to incorporate a few % of Si in these chains[33]. Indeed experiments show that starting with B<sub>13</sub>C<sub>2</sub> and putting 2% Si distributed among the chains leads to improved ductility. We have simulated this by replacing the BC of some chains with Si, totaling 2% and we also find improved ductility[33].

Our studies of brittleness in B<sub>4</sub>C showed that cracking across grains leads to amorphization [24] and we showed that very small grains lead to grain boundaries that direct shear along these boundaries [28]. This was studied in depth in collaboration with Lasalvia [34]. Interestingly, we found that microalloying with Mg also leads to enhanced ductility [35]. This has not yet been tested experimentally.

Summarizing, the theory and simulations have shown that incorporating Si, P, O, and Mg[29, 30, 31, 35] into grain boundaries can improve ductility and current synthesis techniques have demonstrated this experimentally for Si in B rich materials. We suggest that incorporating P should be investigated experimentally.

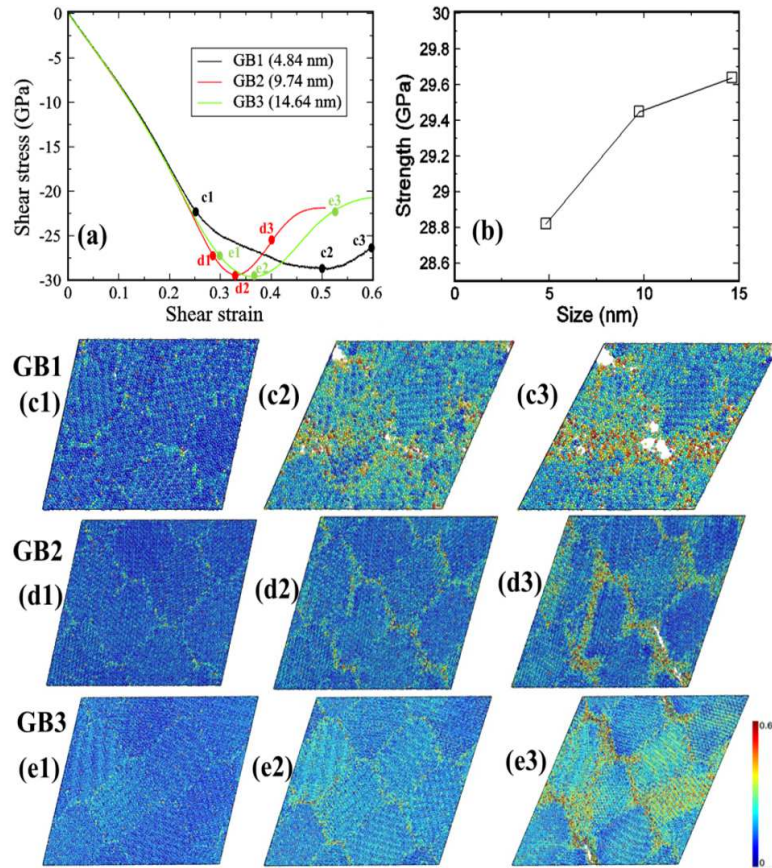


Figure 3: (a) The shear-stress-shear-strain relationships of nano- $B_4C$  for three grain sizes (GB1=5nm, GB2=10nm, GB3=15nm) under ideal shear deformation. (b) The ideal strength vs. grain sizes. (c-e) The snapshots for the three GB models at different stress corresponding to the points in Fig. (a). (c1-e1) The snapshots of the beginning of plastic deformation. (c2-e2) The snapshots with critical shear stress. (c3-e3) The snapshots of formation of cavitation. This figure is from Ref. [28]

### 3.1.2 Continuum models for amorphization

Amorphization is fundamentally a subgrain mechanism, in that it occurs within the crystal. However, most continuum models of ceramics do not account for the grain structure. As a consequence, the development of amorphization within the crystal must be included within a continuum model as an internal state variable that evolves in some way. By definition, a continuum model will not resolve individual amorphous bands and rather must replace them by an equivalent amorphization volume fraction. Therefore, a continuum model must define three things: first, a threshold for the onset of amorphization; second, a criterion for the evolution of the amorphization volume fraction; and third, the properties of the amorphous material.

Amorphization has been observed in a variety of materials other than boron carbide, including silicon, quartz, and other geomaterials, with a variety of crystal structures. Several authors [36, 37, 38, 22] have defined amorphization thresholds using criteria related to the Born instability (based on the anisotropic elastic moduli of the crystals). Such a threshold criterion is useful when the deformation occurs entirely within a single crystal (e.g. nanoindentation). In most continuum simulations of boron carbide under impact, however, the material is polycrystalline. In such cases the representative volume element (RVE) used to define material behavior at a Gauss point in a finite element usually spans hundreds of crystals, and so a Born stability argument cannot be used. In such a case the amorphization threshold criterion can be either stress-based or strain-based, but it is most commonly stress-based (e.g. defining a critical shock stress at which amorphization is assumed to set in, as in the case of quartz [39]). In the case of boron carbide, based on diamond anvil cell experiments, a threshold criterion based on a combination of pressure and shear stress is appropriate [40].

Once amorphization has set in, the degree of amorphization and the behavior of the amorphous material must be defined. The rate of growth of the amorphization volume fraction within the RVE in a continuum model is defined as a function of the stress state [40]. The behavior of the amorphous material is itself described in terms of volumetric and deviatoric behaviors, with a combination of densification within the band and viscoplastic sliding across the band. A review of the corresponding evolution equations and the related experimental data is presented by [40]. The form of the equations is derived from the atomistic simulations combined with available experimental data, and the equations can be parameterized using particle velocity histories from a set of plate impact experiments.

## 3.2 Dynamic fracture of boron carbide

As with all ceramics, the primary failure mode for boron carbide is fracture. In the case of dynamic loading, fracture is observed under all stress states except that of very high pressures. Even under predominantly compressive stress states, wing cracks are observed to nucleate from defects within the material [41, 42], and these cracks can grow rapidly. The primary defects that nucleate such cracks are observed to be carbonaceous defects in commercial boron carbides [43]. Under dynamic loading the majority of the defect population in the boron carbide may nucleate cracks [44, 14], and so the overall response of the material is affected both by crack nucleation and crack growth. Crack growth speeds are high in boron carbide (speeds of 2 km/s have been observed [43, 17, 45]), and longitudinal and shear wave speeds are also very high (given the high modulus and low density). Nevertheless, the finite crack speeds, combined with the defect distributions, lead to an effective rate dependence of the strength of boron carbide [44]. The key mechanism is that of the interaction of dynamically growing cracks, discussed below. Experimental work on the dynamic fracture of boron carbide has been extensive over the last few years, e.g. [43, 17, 45]. One advantage of a subset of the recent experimental literature is that much of the work was performed on samples taken from a single plate of a commercially available material that has been very well characterized [46, 43], thus ensuring relative consistency of the microstructure.

### 3.2.1 Models for dynamic fracture of ceramics

Most models for the dynamic fracture of brittle solids can be related back to the seminal work of Freund [47], and consider the driving force needed for a single crack propagating at constant velocity. These approaches are summarized in books such as that by [48], and are consistent with experimental results. Current work in the area includes the examination of transonic and supersonic cracks [49], but transonic and supersonic cracks have not been observed in boron carbide (the damage fronts observed by [50] do not represent individual crack speeds). Crack growth speeds as high as 2 km/s have been observed in boron carbide [43, 17, 45], but the longitudinal and shear wave speeds in boron carbide are also high, so the observed crack speeds are subsonic. Thus classical dynamic fracture mechanics is appropriate in terms of individual cracks in boron carbide. However, the high compressive stresses generated by the impact result in the nucleation of large numbers of cracks, and so the effective interaction of many dynamically growing cracks is the key mechanism that must be captured. The cracks that are developed in boron carbide under overall dynamic compression are so-called wing cracks [10] nucleated from sliding on thin carbonaceous defects [41, 42]. Given typical defect densities and the number of cracks

nucleated, continuum models for the behavior of boron carbide that include these cracks take the form of damage models, with the damage growth rate determined through micromechanics analyses.

The typical approach within continuum models of dynamic fracture in ceramics is captured within Figure 4. The microstructure of the boron carbide presented in Figure 4a contains a distribution of carbonaceous defects, typically with a plate-like morphology. Each of these defects is typically modeled as a penny-shaped crack as shown in Figure 4b, with each defect having a size  $2s$  and normal  $\mathbf{n}$  (thus the defects are described in terms of a size distribution and an orientation distribution). When the material is subjected to a sufficiently large compressive stress state, sliding can occur across any given defect (which is typically graphitic [27]), resulting in the activation of wing cracks as shown in Figure 4c. The traction vector  $T$  on the defect under any loading results in a maximum shear stress direction, which we denote by  $P$ . Once the wing crack length  $l$  becomes sufficiently large with respect to the defect half-size  $s$ , the mechanics associated with any given defect can be approximated as a 2-dimensional problem as shown in Figure 4d. For this 2D problem of a single sliding defect and if the local stress state is known, the driving force at the crack tip is known in terms of the stress intensity factor  $K_I$  e.g. [10] (we assume the crack is in an opening mode, or mode I, for the purposes of this discussion). However, we do not have a single defect and associated wing cracks, but rather a distribution of these, and the existence of the other cracks will affect the local driving force on any given crack. One approach to addressing these interactions is by assuming that the defects are all of the same size and arranged in an array, e.g. [11]. A more general approach would consider a size distribution of defects that are randomly located in the material as in Figure 4e, and then use a self-consistent approach (Figure 4f) to compute the driving force on the crack tips. This approach was developed for dynamically growing cracks by [44, 14]. Once the driving stress intensity factor is known, the rate of growth of a crack of length  $l(t)$  is given by

$$\dot{l} = c_R f(K_I, K_{IC}) \quad (1)$$

where  $c_R$  is the Rayleigh wave speed and  $K_{IC}$  is the fracture toughness of the material. The function  $f(K_I, K_{IC})$  is typically assumed to be of the form derived by Freund [47], often extended into a power law with two parameters that can be determined from experimental observations of dynamically growing cracks.

Now that the rate of growth of wing cracks from a distribution of defects can be computed, it becomes possible to determine the effective behavior of the ceramic in terms of an effective damage function, the kinematics, and the stress state [51] and this approach has been applied to boron carbide [52], see the detailed explanations therein. The overall model can

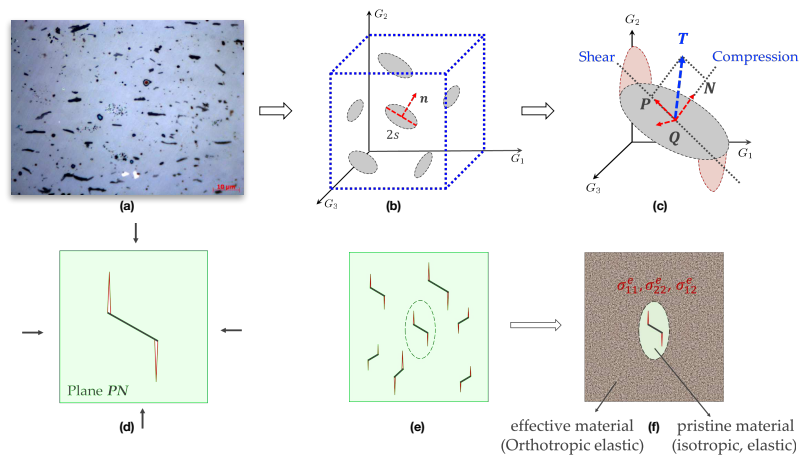


Figure 4: Development of a model for boron carbide containing cracks nucleating from a distribution of processing-induced defects

now make physics-based predictions of the behavior under multiple loading states (e.g., dynamic uniaxial stress and dynamic uniaxial strain) once it is provided with the microstructural parameters and crack speeds needed as inputs. However, note that once the propagating cracks intersect, the system transitions towards a fragmentation rather than a fracture problem, and the fragments eventually lead to a granular material. The next section discusses the transition from fracture to granular flow.

### 3.3 Transition from fracture to granular flow

As cracks in damaged solids grow in length in the presence of macroscopic stress and strain, they interact and begin to coalesce. Cracks initially close to one another often coalesce in different modes [53, 54], leading to larger coalesced crack assemblies and altered crack densities. Huq et. al. [55] developed a crack growth and coalescence model to address this behavior. As cracks grow in length during rapid loading, multiple cracks may also coalesce simultaneously. This type of coalescence, called competitive crack coalescence [56] is challenging to model because explicit representation of all cracks is computationally infeasible. While idealisations of independent crack growth in an effective media is computationally tractable, they do not address the fundamental evolution of the material from a cracked continuum to a fully fragmented solid. Some continuum models describing competitive crack coalescence rely on a gradual transition from a solid to a granular phase based on damage parameters specific to the model [57, 58, 59, 4]. Other models feature a sharp transition based on a critical threshold of energy [60] or a damage parameter [51, 2, 5].

### 3.3.1 Transition model

Bhattacharjee et. al. [61] modelled the instantaneous crack coalescence and fragmentation by discrete simulation of crack populations modeled using a modified version of the Paliwal & Ramesh model [14] with varying initial defect orientation. 3D cracks were modelled in a voxellized space, and crack coalescence was accomplished through a coalescence zone that surrounds a crack. This zone (Figure 5a) represents a probabilistic region in which crack coalescence can occur over a given time step. A connected-region algorithm is used to isolate and extract fragments in a cracked material. This is followed by a dilation procedure to compensate for resolution effect in calculating fragment sizes within a voxellized domain. Figure 5b shows a representative image of a fully fragmented microstructure. The paper establishes a new metric to identify the degree of fragmentation called the Effective Fragmentation Ratio (EFR). Transition to a granular phase occurs when the EFR reaches a critical threshold. Parametric studies of the 3D fragmentation model and a phenomenological model were used to independently establish an empirical, microstructure-dependent transition equation which serves as a switch in continuum damage models to activate granular physics. Implementation of this modified transition criterion in the integrated ceramics model demonstrated more realistic representation of failure patterns in simulations of impact experiments [62].

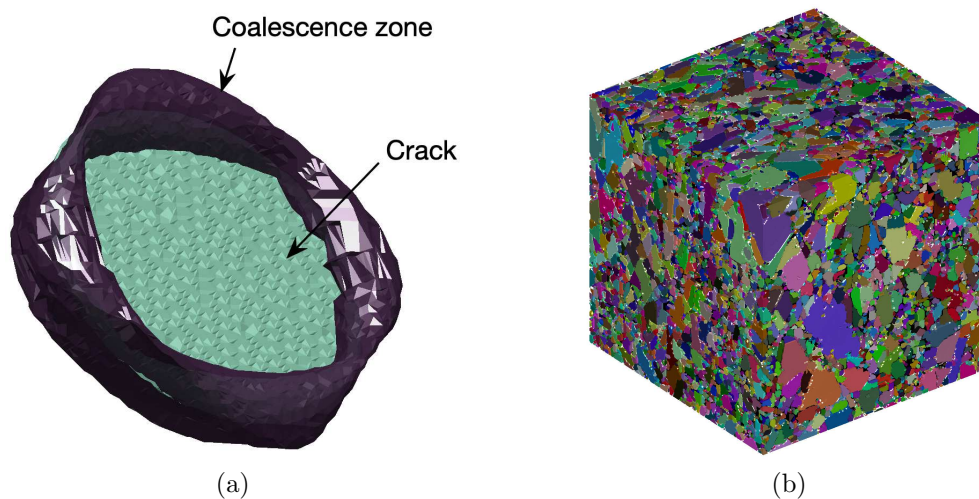


Figure 5: Representative images of (a) a crack with a coalescence zone, (b) a fully fragmented microstructure (Individual fragments are represented by different colors).

Once the transition from fracture to granular behavior is complete, the now granular material (the comminuted ceramic) can flow. We discuss

models for the granular flow of such comminuted ceramics (and boron carbide in particular) in the next section.

### 3.4 Granular flow of comminuted ceramics

In high-rate impact experiments of armor ceramics, the region immediately under the impactor experiences a high degree of fragmentation, resulting in a comminuted zone often referred to as the Mescall region [63, 64, 65, 16, 66]. The macromechanical response of this region is characterized by the kinematics of granular media, or granular flow. Granular flow has been extensively studied in geomechanics [67, 68, 69, 70, 71, 72], astrophysics [73, 74], manufacturing [75, 76, 77], armor ceramics [64, 78, 79]. For armor ceramics, the specific problem of interest is that of dry, dense, high-rate granular flows. Models for granular flow can be broadly classified as particle-based models and continuum-based methods. The choice between these models is related to the required scalability, efficiency and accuracy in capturing the various mechanisms and associated behavior: frictional sliding, particle rearrangement, dilatancy, pore collapse and particle breakage.

#### 3.4.1 Classical models for granular flow

Instead of considering individual particles as ions/molecules (as done in molecular dynamics simulations), particles can also be considered as a specific region of the continuum. Examples of these methods include discrete element models (DEM) [80], material point method [81], and peridynamics [82]. These approaches are generally well-suited to handle discontinuities in fragmentation and granular flow due to their mesh-free nature. To explore the micromechanical dynamics of the transition to granular flow, Clemmer and Robbins studied the breakup and flow of sheared, brittle solids with a focus on the evolution of the distribution of fragment masses [83]. The study used a mix of ideas from DEM and molecular dynamics to simulate large systems capable of resolving several orders of magnitude of fragment sizes. By controlling interactions between particles, the bulk and shear moduli as well as the mode I and II fracture toughness were independently varied. Upon fracturing, a power-law distribution of fragment masses was identified which extended to a maximum cutoff that increased with further strain. A sample set of grains from a fractured system is seen in Figure 6. Simulations characterized the impact of strain, rate, and material properties on this power-law distribution.

Despite their versatility in modelling complicated deformation, particle based models [84] are constrained by the number of particles that can be reasonably simulated. To avoid such restrictions, mesh based continuum models can also be used to study the granular flow mechanism, but they

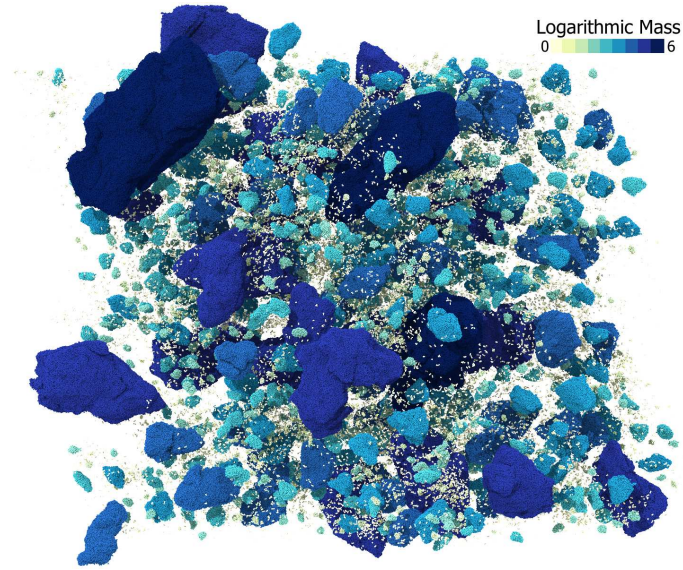


Figure 6: Exploded view of fully fragmented DEM undergoing granular flow. Grains are colored by their logarithmic mass. Grains consisting of a single particle were removed for visibility.

cannot represent fragmentation unless empirical rules are considered for element deletion. The constitutive laws defining the granular flow in conventional mesh based and/or mesh-free based continuum particle methods is typically done using classical plasticity models [57, 5, 85, 86, 87, 88, 89] and micro-mechanics-based kinematic formulations. Micromechanical models provide more physically-realistic approximations of the underlying microscale behaviour averaged over a mesoscale representative volume element (RVE), and they have the capability of simulating more complicated kinematics.

The classical plasticity models differ in their treatment of yield criteria, rate dependency and the flow criterion. In the past, the Tresca yield criterion [90] or a cohesionless Mohr-Coulumb model with shear strength saturation beyond the HEL [85, 91] has been used to model the comminuted region in cavity expansion problems. Numerous viscoplastic granular flow models were developed and employed in literature [51, 86, 57, 2, 4, 92]. In the current continuum implementation of granular flow modeling within the constitutive model, three different options have been implemented for the user [51, 92, 93], which have been discussed later in the manuscript.

FRAGBED models [94, 95, 96] are some of the earliest micromechanical models of granular flow in which the key concepts of dislocation mechanics were utilized to model the porosity evolution and subsequent granular behavior of comminuted ceramics. Another class of micromechanical models are based on continuum breakage mechanics theory first developed by

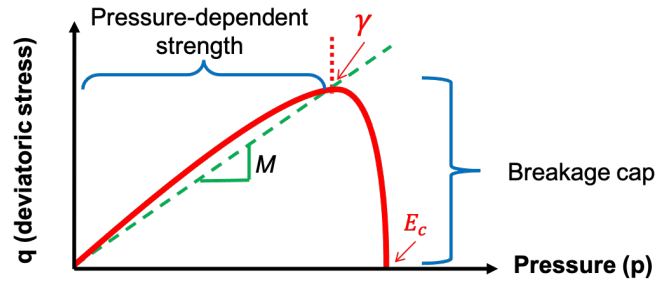


Figure 7: Representative image of the yield surface of the continuum breakage model in the  $p$ - $q$  stress space.

Einav [97, 98, 99]. As part of this work, apart from the implementation of the plasticity based granular flow model [51, 92], a model for granular flow in boron carbide was also implemented referred to as the Breakage model [93].

### 3.4.2 Breakage model for ceramics

Cil et. al. [93] developed a constitutive model for brittle materials that accounts for the competition between dilation and particle breakage, two mechanisms driving the porosity evolution and material deformation. The key premise of this work is that particles undergo refragmentation until they reach a critical distribution. An internal state variable called the breakage parameter quantifies this evolving particle size distribution. The yield surface of the granular material shifts with particle fragmentation. The model formulation takes three primary dissipative mechanisms into account: (a) particle breakage, (b) particle reorganization, (c) frictional sliding. Rate-dependency using the overstress theory of viscoplasticity was further introduced in [100]. The model was calibrated and validated against drained triaxial compression data of different sands and its predictive capabilities were assessed against experimental data on granular ceramics. Further implementation of this model in the framework of an integrated ceramics model in [101, 62] compared performance in simulations of various impact experiments on Boron Carbide against experimental observations.

Figure 7 shows a representative image of the yield surface ( $\gamma$ ) in the pressure ( $p$ )-deviatoric stress ( $q$ ) space. Note this model also represents a capped formulation as that of the previous model used [51]. The green dotted line, with a slope  $M$ , denotes the critical state line.  $M$  is a measure of granular friction and is inherently related to the particle morphology. The intercept on the  $p$ -axis, the critical breakage energy density,  $E_C$ , is the energy density at which particle breakage initiates in the media.

Now that we have described all of the unit mechanisms, we describe how these individual models can be integrated into a holistic constitutive

model for boron carbide.

## 4 Integrated model for boron carbide in extreme dynamic environments

This section describes the integration of the individual mechanisms of amorphization, fracture and granular flow in boron carbide into a single integrative physics-based model that can be used to guide the design of boron carbide for dynamic applications. We refer to this multi-mechanism model henceforth as the “integrated model.” Previously, physics-based models for the fracture and granular flow mechanisms have been incorporated into constitutive models for ceramics by researchers such as Deshpande et al. [57] and Tonge and Ramesh [51]. The latter also incorporated the equation of state, and the pore compaction mechanism. With respect to boron carbide, Tonge and Ramesh [52] provided a nearly complete constitutive model that integrated the equation of state and the mechanisms of pore collapse, dilation, fracture and granular flow, and that could be calibrated using existing experimental data. However, that model could not explain the observed behavior of boron carbide in plate impact experiments [79]. During these uniaxial strain experiments, the fracture mechanism is often suppressed by the confining stresses. Given the lack of experimentally observed slip plasticity in boron carbide, the plate impact experiments could only be explained in terms of the high-pressure amorphization mechanism. This additional mechanism of amorphization was incorporated into an extended integrative model by Zeng, Tonge and Ramesh [40, 102], with the amorphization model parameters calibrated using plate impact experiments. The model can also be calibrated using indentation [40]. Recently Li and Ramesh [103] extended these models to include plasticity and finite deformations, but dislocation plasticity has not been observed to any significant degree in boron carbide. Here we bring these mechanisms together for boron carbide, and show some predictions of the model.

A Mie-Gruneisen equation of state is used in this integrated model for boron carbide. Details regarding the implementation of the equation of state and pore compaction are presented in previous work of Ramesh group [51]. All of the mechanisms, including amorphization, are implemented at the continuum scale, with the general approximation that an RVE in the model represents at least 100 grains. The individual subcomponents of the model are of the forms described above. In the case of granular flow, given the limited available experimental data, three different granular flow models are currently implemented within this integrative model: a two surface plasticity model [51], a one surface tear-drop shaped plasticity model [92] and the breakage model [93]. Details about the individual mechanisms of

the integrative model have been outlined in numerous previous publications [52, 102], and the process of integration of these mechanisms (e.g. for arbitrary stress paths) is described in the work of Zeng et al. [102].

#### 4.1 Calibration of the model

The basic approach to calibrating the model for boron carbide is discussed in detail by Zeng et al. [102]. The input parameters for the model include basic material properties such as the density, specific heat capacity, shear modulus and bulk modulus for the polycrystalline boron carbide as well as the Mie-Gruneisen EoS parameters. The amorphization model parameters can be calibrated by fitting the results of plate impact experiments, since the early time behavior in these experiments is not affected by the fracture or granular flow mechanisms. For the fracture mechanisms and the transition to granular flow, the key information needed is the initial distribution of processing-induced defects (in commercial hot-pressed boron carbides, the relevant defects are carbonaceous inclusions that are larger than the grain size). Generally the size distribution is sufficient if the isotropic damage tensor is used, as in the simulations in this paper. Size and orientation distributions, typically obtained through detail microCT characterization, can be input directly into the model; if such distributions are not available, the distributions can be calibrated by matching the rate-dependent strength under uniaxial stress loading (a dumbbell test [104] would be ideal, but such data is often not available). One input parameter that must often be fit is the friction coefficient associated with sliding in the plane of the defect - in the case of boron carbide, this can be estimated from the properties of graphite. The parameters associated with the equation that defines the crack growth rate (such as crack speed and crack growth exponent) are typically determined directly from crack visualization experiments. Finally, the granular flow parameters must be determined using either literature data (for the case of Drucker-Prager type plasticity) or through independent experiments (if the breakage model of Section 3.4.2 is used). In the set of simulations presented in this manuscript, Drucker-Prager based plasticity model is chosen for representation of the granular flow in the material.

The list of calibrated parameters and their values (for the case of boron carbide) is presented in the table below.

#### 4.2 Implementation of the Integrated model in different codes

The integrated ceramic model was initially developed as a native material model for the Uintah Computational Framework [110]. This framework

EOS	Density ( $\rho$ )	2520 kg/m <sup>3</sup>	[105]
	Specific heat capacity ( $c_v$ )	962 J/(kg·K)	[106]
	Bulk sound speed ( $C_0$ )	$9.6 \times 10^3$ m/s	Calculated
	$U_s - U_p$ slope ( $S$ )	0.914	[106]
	Gruneisen parameter $\Gamma_0$	1.28	[106]
	Shear modulus ( $G_0$ )	197 GPa	[14]
	Bulk modulus ( $K_0$ )	232 GPa	[106]
Amorphization	Initial threshold ( $F_{a0}$ )	50 GPa	[22]
	Shear-enhancement coefficient ( $\alpha$ )	7.63	HEL in [107]
	Density change ( $\eta_a$ )	5%	[25]
	Reference amorphization rate ( $\dot{\xi}_c$ )	1.0	
	Rate sensitivity coefficient ( $m$ )	2	
	Completion stress ( $F_{ac}$ )	400 GPa	Calibrated
	Viscosity of amorphous phase ( $\mu_{band}$ )	1000 Pa·s	Rate-sensitive above $10^6$ s <sup>-1</sup>
	Initial shear resistance ( $\tau_0$ )	7.0 GPa	Shear strength
	Critical failure strain ( $\gamma_{band}^c$ )	0.3	
	Failed-band number density $k_a$	$1.0 \times 10^{23}$ m <sup>-3</sup>	Calibrated
Failed-band number density $n_a$	1		
Energy dissipation rate per band ( $G_c$ )	100 J/m <sup>2</sup>	[108]	
Flaw Distribution	Minimum flaw size ( $s_{min}$ )	1.0 $\mu$ m	
	Maximum flaw size ( $s_{max}$ )	25.0 $\mu$ m	
	Distribution exponent ( $\zeta$ )	2.6	
	Flaw density ( $\eta$ )	$22 \times 10^{12}$ m <sup>-3</sup>	Dynamic strength
Microcracking	Fracture toughness ( $K_{Ic}$ )	$2.5 \text{ MPa}\sqrt{m}$	[44]
	Maximum crack velocity ( $V_m$ )	$0.2 C_r$	[14]
	Crack growth exponent ( $\kappa$ )	1.0	
	Coefficient of friction ( $\mu$ )	0.6	[109]
	Crack orientation ( $\phi$ )	60°	
Granular Plasticity	Activation damage ( $D_c$ )	2.906	
	Frictional slope ( $A_0$ )	0.15	Calibrated
	Purely deviatoric strength ( $Y_0$ )	0 MPa	[87]
	Cohesive strength ( $B_0$ )	3 MPa	[87]
	Reference crush pressure ( $p_0$ )	100 MPa	
	Reference distension ( $J_0^{gp}$ )	2.0	
	Consolidation pressure ( $p_c$ )	30 GPa	
Relaxation time ( $\tau_{gp}$ )	$7.0 \times 10^{-9}$ s	$0.1 \times 10^{-9}$ s for amorphization	

Table 1: Summary of material parameters for BC, slightly modified from those presented earlier [102]

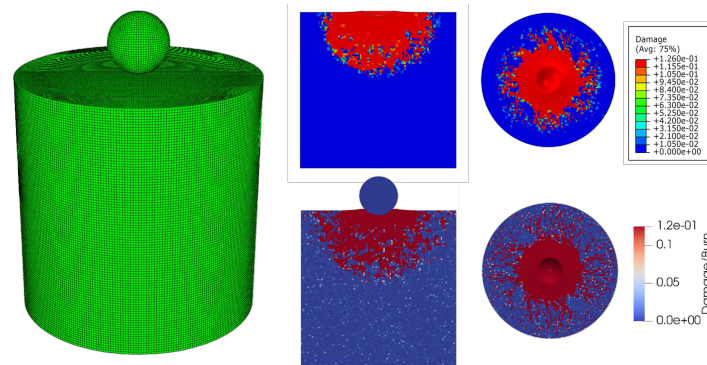


Figure 8: Comparison of resulting damage in Abaqus and EPIC simulations of a sphere impacting boron carbide at 400 m/s. Abaqus simulations are the top row and EPIC simulations are shown in the bottom row.

provided a suitable baseline for initial development and validation of the model[51, 52], but there are several other computational frameworks that can be and are used within production environments. The initial implementation was converted to an Abaqus UMAT through a project with the High Performance Computing Modernization Program (HPCMP) Productivity Enhancement Technology Transfer and Training (PETTT) program[111]. This Abaqus UMAT based model can be used in many production codes used throughout the US Department of Defense (DoD), US Department of Energy (DOE), and Academia including Abaqus [112], Sierra/SM [113], ALEGRA [114], ALE3D [115], and EPIC [116].

The historical model has been implemented as material models in different host codes based on the published model equations by each host code developer. Not only does this approach create inefficiencies by duplicating effort, but it also introduces different implicit assumptions within the model. These differences in assumptions may cause differences in the observed simulation results. When different momentum solvers give different results for the same initial boundary value problem it is important to separate differences due to the approximations within the momentum solver like element types or large deformation treatment, or due to differences in the material model. An additional benefit is that a common material model format facilitates rapid transition of models between different host codes. We note that micromechanics based models like the integrated model are particularly susceptible to advection errors and additional steps can be necessary to correct these errors. Some of the issues related to using this integrated model within an advecting framework are discussed in [117].

Figure 8 shows simulation results from Abaqus and EPIC for the same initial boundary value problem of a WC-Co sphere impacting a cylinder of boron carbide at 400 m/s[102]. The Abaqus results are at the top of the

figure and first appeared in [102]. The simulation results from EPIC are in the bottom row of the figure. The Abaqus results are the damage pattern 1.75  $\mu\text{s}$  after impact and the EPIC results are the damage pattern 2.0  $\mu\text{s}$  after impact. Both damage patterns look qualitatively similar. Minor differences in the damage patterns are results of the different realizations of the initial flaw distribution in the material and possible small differences in the contact algorithms between the two finite element codes. Differences in initial flaw distribution are representative of real differences between different pieces of ceramic taken from the same batch and they are an important characteristic of brittle materials.

### 4.3 Validation of the Integrated model

Validation of the integrated model has been carried out previously in the literature (validation is often first performed for the individual mechanism submodels using experiments only sensitive to one mechanism, such as some plate impact experiments for the case of amorphization). Different mechanisms are known to be activated in plate impact tests on different ceramics (e.g. amorphization for boron carbide and dislocation slip for silicon carbide). Details of the validation of the integrated model for the case of Boron Carbide is presented in [102] using the experiments of Vogler et al. [107, 79] in constant shock, shock release and shock-reshock modes. Note that the amorphization model alone can also be validated using indentation experiments, but the integrated model requires a wider range of experiments in order to validate the other submodels as well as the integration of the submodels [102].

## 5 An application of the integrated model

The integrated model can be applied to any situations involving the dynamic loading of boron carbide, including ballistic impact into boron carbide targets. Note that the nature of the model makes it less suitable for the effective simulation of quasistatic loading problems. A subsequent paper will present the results of simulations of impact in a variety of geometries and initial material microstructures, but for the purposes of this paper we focus primarily on a “canonical” example: a spherical impactor impacting a disk-shaped target made of boron carbide (the simulation configuration is shown before in figure 8 for a thick cylinder and figure 10a for a thin cylinder/disc). These simulations were performed on the Uintah 2.6 platform using the constitutive parameters listed in Table 1 for a specific hot-pressed boron carbide. This particular impact configuration was chosen because it is also being used in an experimental campaign on the same material, and

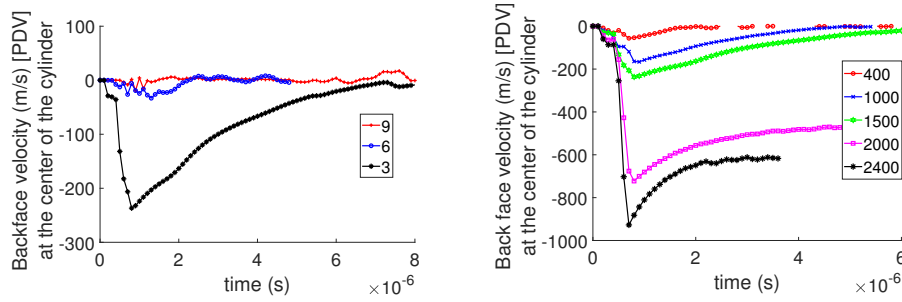


Figure 9: (a) Temporal variation of the particle velocity of the central point (along the shot line) of the rear surface for different target cylinder thicknesses. For these simulations, the target cylinder thickness are in mm; the projectile is 1 mm in diameter and the impact velocity is 1500 m/s. (b) Temporal variation of the particle velocity of the central point (along the shot line) of the rear surface for different target cylinder thicknesses. For these simulations, the impact velocity has been varied and is in m/s, the target cylinder thickness is 3 mm whereas the projectile is 1 mm in diameter. All the above simulations have been carried out using Uintah 2.6 software framework for a boron carbide target and a tungsten carbide spherical projectile

later on newly designed materials (some of which are described in other papers in this journal issue).

The quantities typically measured during such experiments are the impactor velocity, the particle velocity at the rear surface of the target, and the crater/hole sizes and shapes (the latter are measured post-mortem). If flash X-ray imaging is available, one can also visualize the internal damage of the target during the impact process. Simulations are able to access much more information about the impact event, including the full 3D velocity fields, the stress fields, and the evolving damage; but to assess a simulation, one must compare the simulation result with quantities that can be measured within the experiments.

Experimentally, the velocity at a point at the backface of the target plate can be measured using a Photonic Doppler Velocimetry (PDV) sensor. Thus one point of comparison of the simulation and the experiment is the particle velocity at the rear surface. We exercise the integrated model to simulate these impact experiments, and consider first the evolution of the rear surface particle velocity for the case of a tungsten carbide ball (1 mm in diameter) impacting a boron carbide disk at a velocity of  $1500 \text{ m.s}^{-1}$ . One of the strengths of simulations, of course, is that one can explore the parameter space (in this case the target thickness). Figure 9(a) shows the predicted rear surface particle velocity history for this impact configuration, as computed for target thicknesses of 9, 6 and 3 mm. It is immediately

apparent that the model predicts that the rear surface velocity is much larger for the 3 mm thick case, and indeed predicts that the velocity might be below the easily detected range of the PDV system for larger thicknesses. The model predicts that the measured particle velocity will jump to its maximum level over less than a microsecond, and then delay to near zero over 6 microseconds. This provides guidance to the experimental designer. We do not yet have experimental measurements to compare with these simulation results.

The other major control variable in such experiments is the impact velocity. For fixed impactor diameter of 1 mm and fixed target thickness of 3 mm, we have used the integrated model to predict the rear surface particle velocity (the PDV signal) for different impact velocities, and the results are presented in figure 9b. Note that the green line represents the result shown in figure 9a for the 3 mm target thickness. Note the increasing peak velocity, and the rate of increase of the peak velocity - these can also be compared with experimental results as they become available.

Apart from giving us results which can be validated against experimental observations, the integrated model can provide critical insight and information for any given impact configuration (combination of impactor size, impactor velocity, target size, and target material). Such information includes the relative importance of each mechanism, the spatial and temporal evolution of individual mechanisms in the process, as well as the damage in the entire target. This is an important capability because the materials design process involves the control of the microstructure and chemistry, which controls the relative activity of each potential mechanism (the mechanism-based design paradigm that we have discussed previously).

The ability of the integrative model to demonstrate supplementary information which cannot be directly observed from experimental investigations is demonstrated through the example in figure 10. The model can of course also be used to examine other extreme loading situations, to assess the relative importance of individual mechanisms in each situation (and thus provide guidance to materials design for each application).

## 6 Implications for Materials Design

One of the major strengths of developing a mechanism-based integrated model, as demonstrated in the previous section, is the ability to predict which mechanisms are likely to be dominant in specific application configurations. The unit process (mechanism) models then allow one to modify the composition and microstructure of the material so as to control that specific subset of mechanisms, and thus one can design the material for the specific application environment. As we have shown, the amorphiza-

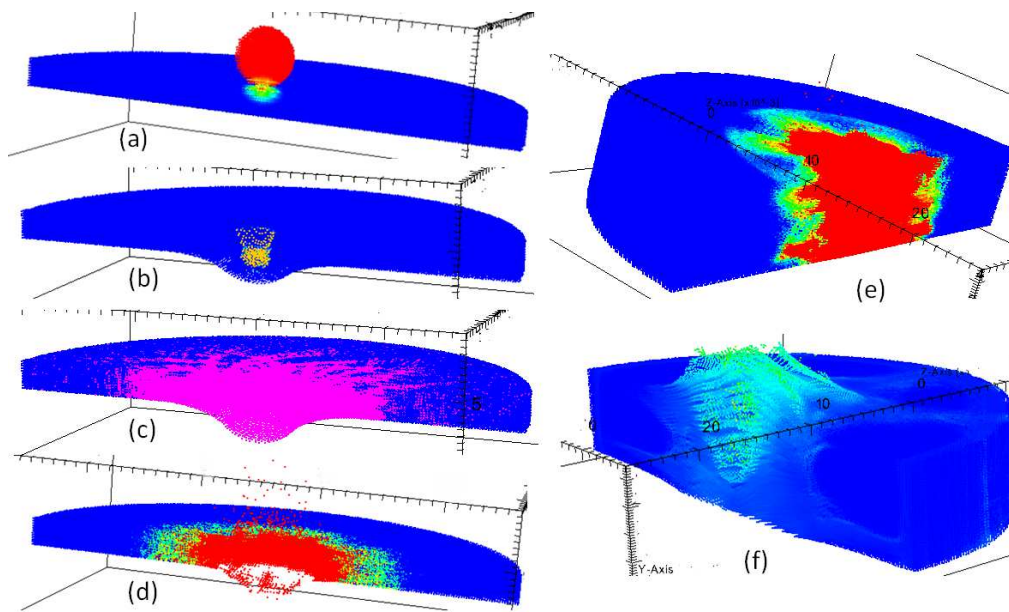


Figure 10: (a) Arrangement of a spherical ball (3 mm projectile) impacting a cylindrical disk (3 mm thick target) [Color represents velocities. Red : projectile with a specified velocity; Blue : target material initially at zero velocity; Green and Yellow colors observed at the point of contact between the projectile and target which lies in between the specified velocity of projectile and zero velocity of target], (b) Amorphization region observed as the impact is made (1 mm projectile impacting a 3 mm target) [Yellow color representing the amorphized zone in the initial target colored blue], (c) Granular flow region observed as the impact is made (1 mm projectile impacting a 3 mm target) [Pink color representing the granular flow region in the initial target colored blue], (d) Complete breakout of 3 mm target plate by a 1 mm projectile at an impact velocity of 2400 m/s (along with ejecta observed at the plate top) [Color coding represents damage variable with red as fully damaged and blue as undamaged; in between colors - green and yellow represents in between damage values], (e) damage region for a 9 mm plate impacted upon by a 1 mm projectile [Color coding represents damage variable with red as fully damaged and blue as undamaged; in between colors - green and yellow represents in between damage values], (f) ejecta observed at the impact surface of a 9 mm plate impacted upon by a 3 mm projectile [color coding represents jacobian of granular flow - the intent here is to show the ejecta shown in lighter colors rising above the surface of the target which is colored blue]. For all the figures, half cylinder is shown for brevity of region demonstration along depth. The target material is boron carbide and projectile is tungsten carbide.

Accepted Article

tion mechanism is primarily controlled by the chemistry and stoichiometry of the boron carbide, while the fracture and fragmentation process is primarily controlled by the distribution of the processing-induced defects in hot-pressed boron carbide. Thus, for an application/target configuration in which amorphization is developed (typically high velocity and highly confined conditions), control of the chemistry and stoichiometry is paramount in order to push back the onset of the amorphization mechanism. However, such stoichiometric control may not gain the designer very much if the application involves lower impact velocities and lower confinement levels, since under those conditions it is the carbonaceous defect distributions that dominate the material behavior (by controlling fracture). The ability of the integrated model to consider the potential competition (and interaction) of these mechanisms is an important factor for materials design. We note that the interactions can be strong: once amorphization sets in (at high velocity and high confinement), the material effectively contains a new population of defects that also affects the subsequent fracture behavior.

## 7 Some open questions

There remains much to be understood about boron carbide, and many directions that are yet to be explored. Experimental measures of amorphization volume fractions under a range of loading conditions are still not available, and the density of the amorphized material needs to be directly measured (rather than inferred). Lacking these key pieces of information, continuum-scale models of amorphization must still be fit to limited experimental data rather than computed from atomistic-scale models. There remains a strong need to connect atomistic simulations to the mechanical response under various loading conditions, particularly off the pressure axis in the deviatoric stress versus hydrostatic stress space. There is also very limited data on the effects of different types of mesoscale defects on mechanical performance under these impact conditions. The potential of grain boundary engineering to affect the dynamic mechanical behavior is also a promising research direction. In terms of granular flow, physics-based approaches such as the breakage model need explicit characterization of fragment size distributions before and after load. Further, under some extreme conditions (e.g. high impact velocities), the thermomechanics of amorphization, fracture and granular flow remain to be explored in depth. Finally, there is a strong need for plate impact experiments on well-characterized boron carbides with known stoichiometry and microstructures.

## 8 Acknowledgments

Research was sponsored by the Army Research Laboratory and was accomplished under Cooperative Agreement Number W911NF-12-2-0022. The views and conclusions contained in this document are those of the authors and should not be interpreted as representing the official policies, either expressed or implied, of the Army Research Laboratory or the U.S. Government. The U.S. Government is authorized to reproduce and distribute reprints for Government purposes notwithstanding any copyright notation herein.

## References

- [1] A. Awasthi and G. Subhash. Deformation behavior and amorphization in icosahedral boron-rich ceramics. *Progress in Materials Science*, 112:100664, 2020.
- [2] G. R. Johnson and T. J. Holmquist. A computational constitutive model for brittle materials subjected to large strains, high strain rates and high pressures. In M. A. Meyers, L. E. Murr, and K. P. Staudhammer, editors, *Shock-wave and High Strain-rate Phenomena in Materials*, pages 1075–1081. Marcel Dekker Inc., 1992.
- [3] G. R. Johnson and T. J. Holmquist. An improved computational constitutive model for brittle materials. *High Pressure Science and Technology*, pages 981–984, 1993.
- [4] G. R. Johnson and T. J. Holmquist. An improved computational constitutive model for brittle materials. *AIP Conference Proceedings*, 309(1):981–984, 1994.
- [5] G. R. Johnson, T. J. Holmquist, and S. R. Beissel. Response of aluminum nitride (including a phase change) to large strains, high strain rates, and high pressures. *Journal of Applied Physics*, 94(3):1639–1646, 2003.
- [6] T.J. Holmquist and G.R. Johnson. Characterization and evaluation of boron carbide for plate-impact conditions. *Journal of Applied Physics*, 100(9), 2006.
- [7] R.M. Brannon, A.F. Fossum, and O.E. Strack. Kayenta: Theory and user’s guide. Technical Report SAND2009-2282, Sandia National Laboratories, 2009.

- Accepted Article
- [8] S. Bavdekar and G. Subhash. Comparison of pressure sensitive strength models for ceramics under ultrahigh confinement. *International Journal of Impact Engineering*, 118:60–66, 2018.
  - [9] M. Shafiq and G. Subhash. An extended mohr-columb model for fracture strength of intact brittle materials under ultrahigh pressures. *Journal of the American Ceramic Society*, 99(2):627–630, 2016.
  - [10] S. Nemat-Nasser and H. Horii. Compression-induced nonplanar crack extension with application to splitting, exfoliation, and rockburst. *Journal of Geophysical Research*, 87(B8):6805–6821, 1982.
  - [11] H. Deng and S. Nemat-Nasser. Microcrack arrays in isotropic solids. *Mechanics of Materials*, 13(1):15–36, 1992.
  - [12] S. Nemat-Nasser and M. Obata. Microcrack model of dilatancy in brittle materials. *Journal of Applied Mechanics, Transactions ASME*, 55(1):24–35, 1988.
  - [13] C. Huang and Subhash G. Influence of lateral confinement on dynamic damage evolution during uniaxial compressive response of brittle solids. *Journal of the Mechanics and Physics of Solids*, 51(6):1089 – 1105, 2003.
  - [14] B. Paliwal and K.T. Ramesh. An interacting micro-crack damage model for failure of brittle materials under compression. *Journal of the Mechanics and Physics of Solids*, 56(3):896 – 923, 2008.
  - [15] M. Chen, J. W. McCauley, and K. J. Hemker. Shock-induced localized amorphization in boron carbide. *Science*, 299(5612):1563–1566, 2003.
  - [16] J. C. LaSalvia, M. J. Normandia, H. T. Miller, and D. E. MacKenzie. *Sphere Impact Induced Damage in Ceramics: II. Armor-Grade B<sub>4</sub>C and WC*, chapter 21, pages 183–192. John Wiley & Sons, Ltd, 2005.
  - [17] J.D. Hogan, L. Farbaniec, D. Mallick, V. Domnich, K. Kuwelkar, T. Sano, J.W. MaCauley, and K.T. Ramesh. Fragmentation of an advanced ceramic under ballistic impact: Mechanisms and microstructure. *International Journal of Impact Engineering*, 102:47 – 54, 2017.
  - [18] A. Awasthi and G. Subhash. High pressure deformation and amorphization in boron carbide. *Journal of Applied Physics*, 125:215901, 2019.
  - [19] M. DeVries, G. Subhash, and A. Awasthi. Shocked ceramics melt: An atomistic analysis of thermodynamic behavior of boron carbide. *Physical Review B*, 101:144107, 2020.

- [20] S. Aryal, P. Rulis, and W. Y. Ching. Mechanism for amorphization of boron carbide  $b_4c$  under uniaxial compression. *Physical Review B*, 84:184112, Nov 2011.
- [21] X. Q. Yan, Z. Tang, L. Zhang, J. J. Guo, C. Q. Jin, Y. Zhang, T. Goto, J. W. McCauley, and M. W. Chen. Depressurization amorphization of single-crystal boron carbide. *Physical Review Letters*, 102:075505, Feb 2009.
- [22] D. E. Taylor. Shock compression of boron carbide: A quantum mechanical analysis. *Journal of the American Ceramic Society*, 98(10):3308–3318.
- [23] K. M. Reddy, P. Liu, A. Hirata, T. Fujita, and M.W. Chen. Atomic structure of amorphous shear bands in boron carbide. *Nature Communications*, 4:2483.
- [24] Q. An, W. A. Goddard, and T. Cheng. Atomistic explanation of shear-induced amorphous band formation in boron carbide. *Physical Review Letters*, 113:095501, Aug 2014.
- [25] Q. An and W. A. Goddard. Atomistic origin of brittle failure of boron carbide from large-scale reactive dynamics simulations: Suggestions toward improved ductility. *Physical Review Letters*, 115:105501, Aug 2015.
- [26] M. W. Chen, J. W. McCauley, J. C. LaSalvia, and K. J. Hemker. Microstructural characterization of commercial hot-pressed boron carbide ceramics. *Journal of the American Ceramic Society*, 88(7):1935–1942.
- [27] K. Y. Xie, K. Kuwelkar, R. A. Haber, J. C. LaSalvia, and K. J. Hemker. Microstructural characterization of a commercial hot-pressed boron carbide armor plate. *Journal of the American Ceramic Society*, 99(8):2834–2841.
- [28] D. Guo, S. Song, R. Luo, W. A. Goddard, M. Chen, K. M. Reddy, and Q. An. Grain boundary sliding and amorphization are responsible for the reverse hall-petch relation in superhard nanocrystalline boron carbide. *Physical Review Letter*, 121:145504, Oct 2018.
- [29] Q. An and W. A. Goddard. Ductility in crystalline boron subphosphide ( $b_{12}p_2$ ) for large strain indentation. *The Journal of Physical Chemistry C*, 121(30):16644–16649, 2017.

- [30] B. Tang, Q. An, and W. A. Goddard. Improved ductility of boron carbide by microalloying with boron suboxide. *The Journal of Physical Chemistry C*, 119(43):24649–24656, 2015.
- [31] X. Yang, W. A. Goddard, and Q. An. Structure and properties of boron-very-rich boron carbides: B<sub>12</sub> icosahedra linked through bent cbb chains. *The Journal of Physical Chemistry C*, 122(4):2448–2453, 2018.
- [32] X. Yang, S. P. Coleman, J. C. LaSalvia, W. A. Goddard, and Q. An. Shear-induced brittle failure along grain boundaries in boron carbide. *ACS Applied Materials & Interfaces*, 10(5):5072–5080, 2018. PMID: 29346723.
- [33] A. U. Khan, A. M. Etzold, X. Yang, V. Domnich, K. Y. Xie, C. Hwang, K. D. Behler, M. Chen, Q. An, J. C. LaSalvia, K. J. Hemker, W. A. Goddard, and R. A. Haber. Locating si atoms in si-doped boron carbide: A route to understand amorphization mitigation mechanism. *Acta Materialia*, 157:106–113, 2018.
- [34] B. Tang, Y. He, W. A. Goddard III, and Q. An. First principles predicting enhanced ductility of boride carbide through magnesium microalloying. *Journal of the American Ceramic Society*, 102(9):5514–5523, 2019.
- [35] Q. An, W. A. Goddard, K. Y. Xie, G.D. Sim, K. J. Hemker, T. Munhollon, M. F. Toksoy, and R. A. Haber. Superstrength through nanotwinning. *Nano Letters*, 16(12):7573–7579, 2016. PMID: 27960511.
- [36] J. D. Clayton. Towards a nonlinear elastic representation of finite compression and instability of boron carbide ceramic. *Philosophical Magazine*, 92(23):2860–2893, 2012.
- [37] J. D. Clayton. Mesoscale modeling of dynamic compression of boron carbide polycrystals. *Mechanics Research Communications*, 49:57–64, 2013.
- [38] J. D. Clayton and A. L. Tonge. A nonlinear anisotropic elastic–inelastic constitutive model for polycrystalline ceramics and minerals with application to boron carbide. *International Journal of Solids and Structures*, 64-65:191–207, 2015.
- [39] Q. Zeng, J.W. McCauley, and K.T. Ramesh. A mechanism based model for the impact response of quartz. *Journal of Geophysical Research: Solid Earth*, 126(3):e2020JB020209, 2021.

- Accepted Article
- [40] Q. Zeng, A.L. Tonge, and K.T. Ramesh. A multi-mechanism constitutive model for the dynamic failure of quasi-brittle materials. part I: Amorphization as a failure mode. *Journal of the Mechanics and Physics of Solids*, 130:370–392, 2019.
  - [41] L. Farbaniec, J.D. Hogan, and K.T. Ramesh. Micromechanisms associated with the dynamic compressive failure of hot-pressed boron carbide. *Scripta Materialia*, 106:52 – 56, 2015.
  - [42] L. Farbaniec, J.D. Hogan, K.Y. Xie, M. Shaeffer, K.J. Hemker, and K.T. Ramesh. Damage evolution of hot-pressed boron carbide under confined dynamic compression. *International Journal of Impact Engineering*, 99:75 – 84, 2017.
  - [43] J.D. Hogan, L. Farbaniec, T. Sano, M. Shaeffer, and K.T. Ramesh. The effects of defects on the uniaxial compressive strength and failure of an advanced ceramic. *Acta Materialia*, 102:263 – 272, 2016.
  - [44] B. Paliwal and K.T. Ramesh. Effect of crack growth dynamics on the rate-sensitive behavior of hot-pressed boron carbide. *Scripta Materialia*, 57(6):481–484, 2007.
  - [45] J.D. Hogan, L. Farbaniec, M. Shaeffer, and K.T. Ramesh. The effects of the microstructure and confinement on the compressive fragmentation of an advanced ceramic. *Journal of the American Ceramic Society*, 98(3):902 – 912, 2015.
  - [46] L. Farbaniec, J.W. McCauley, J.D. Hogan, and K.T. Ramesh. Anisotropy of mechanical properties in a hot-pressed boron carbide. *International Journal of Applied Ceramic Technology*, 13:1 – 9, 2016.
  - [47] L.B. Freund. Crack propagation in an elastic solid subjected to general loading-II. non-uniform rate of extension. *Journal of the Mechanics and Physics of Solids*, 20(3):141–152, 1972.
  - [48] B.K. Broberg. *Cracks and Fracture*. Academic Press, 1999.
  - [49] A.J. Rosakis, O. Samudrala, and D. Coker. Cracks faster than the shear wave speed. *Science*, 284(5418):1337–1340, 1999.
  - [50] E. Strassburger. Visualization of impact damage in ceramics using the edge-on impact technique. *International Journal of Applied Ceramic Technology*, 1(3):235–242, 2004.
  - [51] A.L. Tonge and K.T. Ramesh. Multi-scale defect interactions in high-rate brittle material failure. part i: Model formulation and application to alon. *Journal of the Mechanics and Physics of Solids*, 86:117 – 149, 2016.

- Accepted Article
- [52] A.L. Tonge and K.T. Ramesh. Multi-scale defect interactions in high-rate failure of brittle materials, part ii: Application to design of protection materials. *Journal of the Mechanics and Physics of Solids*, 86:237–258, January 2016.
  - [53] R.H.C. Wong and K.T. Chau. Crack coalescence in a rock-like material containing two cracks. *International Journal of Rock Mechanics and Mining Sciences*, 35(2):147 – 164, 1998.
  - [54] L. Taoying and C. Ping. Failure Mechanisms of Brittle Rocks under Uniaxial Compression . *Journal of Theoretical and Applied Mechanics*, 47:59, 2020-02-12T17:25:13.677+01:00 2017.
  - [55] F. Huq, J. Liu, A.L. Tonge, and L. Graham-Brady. A micromechanics based model to predict micro-crack coalescence in brittle materials under dynamic compression. *Engineering Fracture Mechanics*, 217:106515, 2019.
  - [56] R.H.C. Wong, K.T. Chau, C.A. Tang, and P. Lin. Analysis of crack coalescence in rock-like materials containing three flaws - Part I: Experimental approach. *International Journal of Rock Mechanics and Mining Sciences*, 38(7):909–924, 10 2001.
  - [57] V.S. Deshpande, E. A. N. Gamble, B. G. Compton, R. M. McMeeking, A. G. Evans, and F. W. Zok. A Constitutive Description of the Inelastic Response of Ceramics. *Journal of the American Ceramic Society*, 94(s1):s204–s214, 2011.
  - [58] V. Lyakhovsky, Y. Hamiel, and Y. Ben-Zion. A non-local visco-elastic damage model and dynamic fracturing. *Journal of the Mechanics and Physics of Solids*, 59(9):1752 – 1776, 2011.
  - [59] V. Lyakhovsky and Y. Ben-Zion. Damage–breakage rheology model and solid-granular transition near brittle instability. *Journal of the Mechanics and Physics of Solids*, 64:184 – 197, 2014.
  - [60] F. Kun and H. J. Herrmann. Transition from damage to fragmentation in collision of solids. *Physical Review E*, 59:2623–2632, Mar 1999.
  - [61] A. Bhattacharjee, R. Hurley, and L. Graham-Brady. Predicting high rate granular transition and fragment statistics at the onset of granular flow for brittle ceramics, Nov 2020. arXiv:2011.08331.
  - [62] A. Bhattacharjee, A. Bhaduri, R. Hurley, and L. Graham-Brady. Failure modelling and sensitivity analysis of ceramics under impact. *Journal of Applied Mechanics*, 88, 2021.

- [63] J. Mescall and V. Weiss. *Material behavior under high stress and ultrahigh loading rates*, volume 29. Springer, 1983.
- [64] D. A. Shockey, A.H. Marchand, S.R. Skaggs, G.E. Cort, M.W. Burckett, and R. Parker. Failure phenomenology of confined ceramic targets and impacting rods. *International Journal of Impact Engineering*, 9(3):263 – 275, 1990.
- [65] R.L. Woodward, W.A. Gooch, R.G. O’Donnell, W.J. Perciballi, B.J. Baxter, and S.D. Pattie. A study of fragmentation in the ballistic impact of ceramics. *International Journal of Impact Engineering*, 15(5):605–618, 1994.
- [66] R. B. Leavy, R. M. Brannon, and O. E. Strack. The Use of Sphere Indentation Experiments to Characterize Ceramic Damage Models. *International Journal of Applied Ceramic Technology*, 7(5):606–615, 2010.
- [67] L-B. Tremblay and L. A. Mysak. Modeling sea ice as a granular material, including the dilatancy effect. *Journal of Physical Oceanography*, 27(11):2342 – 2360, 1997.
- [68] Y. Ben-Zion and C. G. Sammis. Characterization of Fault Zones. *Pure and Applied Geophysics*, 160:677–715, 2003.
- [69] S. Dartevelle. Numerical modeling of geophysical granular flows: 1. A comprehensive approach to granular rheologies and geophysical multiphase flows. *Geochemistry, Geophysics, Geosystems*, 5(8), 2004.
- [70] M. Bursik, A. Patra, E. B. Pitman, C. Nichita, J. L. Macias, R. Saucedo, and O. Girina. Advances in studies of dense volcanic granular flows. *Reports on Progress in Physics*, 68(2):271–301, jan 2005.
- [71] K. Hutter. Geophysical granular and particle-laden flows: review of the field. *Philosophical Transactions of the Royal Society A: Mathematical, Physical and Engineering Sciences*, 363(1832):1497–1505, 2005.
- [72] D. L. Feltham. Granular flow in the marginal ice zone. *Philosophical Transactions of the Royal Society A: Mathematical, Physical and Engineering Sciences*, 363(1832):1677–1700, 2005.
- [73] N. Murdoch, B. Rozitis, S. F. Green, T. L. de Lophem, P. Michel, and W. Losert. Granular shear flow in varying gravitational environments. *Granular Matter*, 15:129–137, 2013.

- [74] D.J. Scheeres, C.M. Hartzell, P. Sánchez, and M. Swift. Scaling forces to asteroid surfaces: The role of cohesion. *Icarus*, 210(2):968–984, 2010.
- [75] J.M.N.T. Gray. Granular flow in partially filled slowly rotating drums. *Journal of Fluid Mechanics*, 441:1–29, 2001.
- [76] M. Ramaioli. *Granular flow simulations and experiments for the food industry*. PhD thesis, École polytechnique fédérale de Lausanne, 2008.
- [77] R. B. Shah, M. A. Tawakkul, and M. A. Khan. Comparative evaluation of flow for pharmaceutical powders and granules. *AAPS Pharm-SciTech*, 9:250–258, 2008.
- [78] X. Sun, A. Chauhan, D. D. Mallick, A. L. Tonge, J. W. McCauley, K. J. Hemker, J. C. LaSalvia, and K.T. Ramesh. Granular flow of an advanced ceramic under ultra-high strain rates and high pressures. *Journal of the Mechanics and Physics of Solids*, 143:104031, 2020.
- [79] T.J. Vogler, M.Y. Lee, and D.E. Grady. Static and dynamic compaction of ceramic powders. *International Journal of Solids and Structures*, 44(2):636–658, 2007.
- [80] H. A. Carmona, F. K. Wittel, F. Kun, and H. J. Herrmann. Fragmentation processes in impact of spheres. *Physical Review E*, 77(5):051302, may 2008.
- [81] M. A. Homel and E. B. Herbold. Field-gradient partitioning for fracture and frictional contact in the material point method. *International Journal for Numerical Methods in Engineering*, 109(7):1013–1044, feb 2017.
- [82] S. A. Silling, C. Barr, M. Cooper, J. Lechman, and D. C. Bufford. Inelastic peridynamic model for molecular crystal particles. *Computational Particle Mechanics*, 2021.
- [83] J. T. Clemmer. *An improved computational constitutive model for brittle materials*. PhD thesis, Johns Hopkins University, 2019.
- [84] Alberto Di Renzo and Francesco Paolo Di Maio. Comparison of contact-force models for the simulation of collisions in DEM-based granular flow codes. *Chemical Engineering Science*, 59(3):525–541, 2004.
- [85] S. Satapathy. Dynamic spherical cavity expansion in brittle ceramics. *International Journal of Solids and Structures*, 38(32):5833–5845, 2001.

- [86] H.D. Espinosa and B.A. Gailly. Modeling of shear instabilities observed in cylinder collapse experiments performed on ceramic powders. *Acta Materialia*, 49(19):4135–4147, 2001.
- [87] S. Chocron, C. E. Anderson Jr., K. A. Dannemann, A. E. Nicholls, and N. L. King. Intact and Predamaged Boron Carbide Strength under Moderate Confinement Pressures. *Journal of the American Ceramic Society*, 95(1):350–357, 2012.
- [88] T. J. Holmquist and G. R. Johnson. The failed strength of ceramics subjected to high-velocity impact. *Journal of Applied Physics*, 104(1):013533, 2008.
- [89] D. H. Zeuch, J. M. Grazier, J. G. Argüello, and K. G. Ewsuk. Mechanical properties and shear failure surfaces for two alumina powders in triaxial compression. *Journal of Materials Science*, 36:2911–2924, 2001.
- [90] J. D. Walker and C. E. Anderson. A time-dependent model for long-rod penetration. *International Journal of Impact Engineering*, 16(1):19–48, 1995.
- [91] S. Bavdekar, G. Subhash, and S. Satapathy. A unified model for dwell and penetration during long rod impact on thick ceramic targets. *International Journal of Impact Engineering*, 131:304–316, 2019.
- [92] C.D. Foster, R.A. Regueiro, A.F. Fossum, and R.I. Borja. Implicit numerical integration of a three-invariant, isotropic/kinematic hardening cap plasticity model for geomaterials. *Computer Methods in Applied Mechanics and Engineering*, 194(50):5109–5138, 2005.
- [93] M. B. Cil, R. C. Hurley, and L. Graham-Brady. Constitutive Model for Brittle Granular Materials Considering Competition between Breakage and Dilation. *Journal of Engineering Mechanics*, 146(1), 2020.
- [94] D.R. Curran, L. Seaman, and D.A. Shockey. Dynamic failure of solids. *Physics Reports*, 147(5):253–388, 1987.
- [95] D.R. Curran, L. Seaman, T. Cooper, and D.A. Shockey. Micromechanical model for comminution and granular flow of brittle material under high strain rate application to penetration of ceramic targets. *International Journal of Impact Engineering*, 13(1):53 – 83, 1993.
- [96] D.R. Curran and T. Cooper. Modeling the comminution and flow of granular brittle material. *J. Phys. IV France*, 110:45 – 50, 2003.

- [97] I. Einav. Breakage mechanics—Part I: Theory. *Journal of the Mechanics and Physics of Solids*, 55(6):1274 – 1297, 2007.
- [98] I. Einav. Breakage mechanics—Part II: Modelling granular materials. *Journal of the Mechanics and Physics of Solids*, 55(6):1298 – 1320, 2007.
- [99] I. Einav. Fracture propagation in brittle granular matter. *Proceedings of the Royal Society A: Mathematical, Physical and Engineering Sciences*, 463(2087):3021–3035, 2007.
- [100] M. B. Cil, R. C. Hurley, and L. Graham-Brady. A rate-dependent constitutive model for brittle granular materials based on breakage mechanics. *Journal of the American Ceramic Society*, 102(9):5524–5534, 2019.
- [101] M. B. Cil, Q. Zeng, R. C. Hurley, and L. Graham-Brady. An Integrative Model for the Dynamic Behavior of Brittle Materials Based on Microcracking and Breakage Mechanics. *Journal of Dynamic Behavior of Materials*, 2020.
- [102] Q. Zeng, A.L. Tonge, and K.T. Ramesh. A multi-mechanism constitutive model for the dynamic failure of quasi-brittle materials. part II: Integrative model. *Journal of the Mechanics and Physics of Solids*, 131:20–42, 2019.
- [103] W. Li and K.T. Ramesh. A finite deformation framework for mechanism-based constitutive models of the dynamic behavior of brittle materials. *Journal of Mechanics and Physics of Solids*, under review, 2021.
- [104] J.J. Swab, C.S. Meredith, D.T. Casem, and W.R. Gamble. Static and dynamic compression strength of hot-pressed boron carbide using a dumbbell shaped specimen. *Journal of Materials Science*, 52:10073 – 10084, 2017.
- [105] F. Thévenot. Boron carbide - A comprehensive review. *Journal of the European Ceramic Society*, 6(4):205–225, 1990.
- [106] D. P. Dandekar. Shock response of boron carbide. Technical Report ARL-TR-2456, Army Research Laboratory, Aberdeen Proving Ground, MD, 2001.
- [107] T. J. Vogler, W. D. Reinhart, and L. C. Chhabildas. Dynamic behavior of boron carbide. *Journal of Applied Physics*, 95(8):4173–4183, 2004.

- [108] D. E. Grady. Adiabatic shear failure in brittle solids. *International Journal of Impact Engineering*, 38(7):661–667, 2011.
- [109] V. Deshpande and A. Evans. Inelastic deformation and energy dissipation in ceramics: A mechanism-based constitutive model. *Journal of the Mechanics and Physics of Solids*, 56(10):3077–3100, 2008.
- [110] J. Davison de St. Germain, J. McCorquodale, S. G. Parker, and C. R. Johnson. Uintah: a massively parallel problem solving environment. *IEEE International Symposium on High Performance Distributed Computing, Proceedings*, pages 33–41, 2000.
- [111] A.L. Tonge. Documentation of the tonge-ramesh material model for release 2015-06-05-152756. Special Report ARL-SR-0344, Army Research Laboratory, October 2015.
- [112] Simula, Hibbit, Karlsson & Sorensen, Inc., 1080 Main St., Pawtucket, RI, 02860-4847. *Abaqus Analysis User's Manual*, version 6.8 edition, April 2008.
- [113] M. T. Merewether, N. K. Crane, G. J. de Frias, S. Le, D. J. Littlewood, M. D. Mosby, K. H. Pierson, V. L. Porter, T. Shelton, J. D. Thomas, M. R. Tupek, M. Veilleux, S. Gampert, P. G. Xavier, and J. A. Plews. Sierra/solid mechanics 4.48 user's guide. 3 2018.
- [114] A. Robinson, T. Brunner, S. Carroll, R. Drake, C. Garasi, T. Gardiner, T. Haill, H. Hanshaw, D. Hensinger, D. Labreche, R. Lemke, E. Love, C. Luchini, S. Mosso, J. Niederhaus, C. Ober, S. Petney, W. Rider, G. Scovazzi, O. Strack, R. Summers, T. Trucano, V. Weirs, M. Wong, and T. Voth. *ALEGRA: An Arbitrary Lagrangian-Eulerian Multimaterial, Multiphysics Code*.
- [115] C. Noble, A. Anderson, N. Barton, J. Bramwell, A. Capps, M. Chang, J. Chou, D. Dawson, E. Diana, T. Dunn, D. Faux, A. Fisher, P. Greene, I. Heinz, Y. Kanarska, S. Khairallah, B. Liu, J. Margraf, A. Nichols, R. Nourgaliev, M. Puso, J. Reus, P. Robinson, A. Shestakov, J. Solberg, D. Taller, P. Tsuji, C. White, and J. White. ALE3D: An arbitrary lagrangian-eulerian multi-physics code. Technical Report LLNL-TR-732040, Lawrence Livermore National Laboratory.
- [116] G.R. Johnson. Numerical algorithms and material models for high-velocity impact computations. *International Journal of Impact Engineering*, 38(6):456–472, 2011. Hypervelocity Impact selected papers from the 2010 Symposium.

[117] A.L. Tonge. Enhancements to the tonge-ramesh ceramic failure model for use in eulerian simulations. Technical Report ARL-TR-7766, Army Research Laboratory, September 2016.

## List of Figures

1	(a) The structures of $B_4C$ at various strains from DFT calculations, showing the Isosurface of the electron localization functional (ELF). At 0.245 strain, the B-C bond connecting two icosahedra breaks, leading to formation of a negative carbene. At 0.348 strain, this negative carbene reacts with the positive Lewis acidic B atom in the middle of C-B-C chain that has bent way over toward the Carbene C due to the large shear. The green and brown balls represent the boron and carbon atoms, respectively. This figure is from ref.[24]. . . . .	5
2	Shear-stress-shear-strain relationship of $B_4C$ [of form $(B_{11}C_p)(CBC)$ ] from ReaxFF reactive Molecular Dynamics (RMD) on a single crystal with dimensions of $\sim 25nm$ (200,000 atoms) (a) shear along $(0001)/[10\bar{1}0]$ ; (b)-(g) snapshots during shearing: (b) Twin formation. (c) Twin growth and new twin formation. (d) The growth of the two twins to the whole cell. (e) formation of the 2-3nm Amorphous shear band within the twinned region. (f) Cavitation within the amorphous band. (g) Full crack formation. This figure is from ref.[25]. . . . .	7
3	(a) The shear-stress-shear-strain relationships of nano- $B_4C$ for three grain sizes (GB1=5nm, GB2=10nm, GB3=15nm) under ideal shear deformation. (b) The ideal strength vs. grain sizes. (c-e) The snapshots for the three GB models at different stress corresponding to the points in Fig. (a). (c1-e1) The snapshots of the beginning of plastic deformation. (c2-e2) The snapshots with critical shear stress. (c3-e3) The snapshots of formation of cavitation. This figure is from Ref. [28] . . . . .	9
4	Development of a model for boron carbide containing cracks nucleating from a distribution of processing-induced defects . . . . .	13
5	Representative images of (a) a crack with a coalescence zone, (b) a fully fragmented microstructure (Individual fragments are represented by different colors). . . . .	14

6	Exploded view of fully fragmented DEM undergoing granular flow. Grains are colored by their logarithmic mass. Grains consisting of a single particle were removed for visibility. . . . .	16
7	Representative image of the yield surface of the continuum breakage model in the p-q stress space. . . . .	17
8	Comparison of Abaqus and EPIC simulations of sphere impact	21
9	(a) Temporal variation of the particle velocity of the central point (along the shot line) of the rear surface for different target cylinder thicknesses. For these simulations, the target cylinder thickness are in mm; the projectile is 1 mm in diameter and the impact velocity is 1500 m/s. (b) Temporal variation of the particle velocity of the central point (along the shot line) of the rear surface for different target cylinder thicknesses. For these simulations, the impact velocity has been varied and is in m/s, the target cylinder thickness is 3 mm whereas the projectile is 1 mm in diameter. All the above simulations have been carried out using Uintah 2.6 software framework for a boron carbide target and a tungsten carbide spherical projectile . . . . .	23

- 10 (a) Arrangement of a spherical ball (3 mm projectile) impacting a cylindrical disk (3 mm thick target) [Color represents velocities. Red : projectile with a specified velocity; Blue : target material initially at zero velocity; Green and Yellow colors observed at the point of contact between the projectile and target which lies in between the specified velocity of projectile and zero velocity of target], (b) Amorphization region observed as the impact is made (1 mm projectile impacting a 3 mm target) [Yellow color representing the amorphized zone in the initial target colored blue], (c) Granular flow region observed as the impact is made (1 mm projectile impacting a 3 mm target) [Pink color representing the granular flow region in the initial target colored blue], (d) Complete breakout of 3 mm target plate by a 1 mm projectile at an impact velocity of 2400 m/s (along with ejecta observed at the plate top) [Color coding represents damage variable with red as fully damaged and blue as undamaged; in between colors - green and yellow represents in between damage values], (e) damage region for a 9 mm plate impacted upon by a 1 mm projectile [Color coding represents damage variable with red as fully damaged and blue as undamaged; in between colors - green and yellow represents in between damage values], (f) ejecta observed at the impact surface of a 9 mm plate impacted upon by a 3 mm projectile [color coding represents jacobian of granular flow - the intent here is to show the ejecta shown in lighter colors rising above the surface of the target which is colored blue]. For all the figures, half cylinder is shown for brevity of region demonstration along depth. The target material is boron carbide and projectile is tungsten carbide. . . . . 25

## List of Tables

- 1 Summary of material parameters for BC, slightly modified from those presented earlier [102] . . . . . 20